Effects of rotation and buoyancy forces on the flow field behavior inside a triangular rib roughened channel

Published
DOI:10.1115/1.4035103

Effects of Rotation and Buoyancy Forces on the Flow Field Behavior Inside a Triangular Rib Roughened Channel

By: Luca Furlani, Alessandro Armellini, Luca Casarsa

Dep. of Electric, Management and Mechanical Engineering – University of Udine –Udine – Italy

Corresponding author: luca.casarsa@uniud.it

ABSTRACT

The flow field inside a triangular cooling channel for the leading edge of a gas turbine blade has been investigated. The efforts were focused on the investigation of the interaction between effects of rotation, of buoyancy forces, and those induced by turbulence promoters, i.e. perpendicular square ribs placed on both leading and trailing sides of the duct. PIV and Stereo-PIV measurements have been performed for $Re_{Dh}=10^4$, rotation number of 0, 0.2, and 0.6, and buoyancy parameter equal to 0, 0.08, and 0.7. Coriolis secondary flows are detected in the duct cross section, but contrary to the smooth case, they are characterized by a single main vortex and are less affected by an increase of the rotation parameter. Moreover, their main topology is only marginally sensitive to the buoyancy forces. Conversely, the features of the recirculation structure downstream the ribs turned out to be more sensitive to both the buoyancy forces and to the stabilizing/de-stabilizing effect on the separated shear layer induced by rotation.

Keywords: blade cooling, internal cooling, rotating channel, buoyancy, rotational effects, PIV

NOMENCLATURE

A	channel cross sectional area without ribs
Bo	buoyancy parameter
Bo_x	buoyancy parameter at a defined x (radial) position
$D_h = 4A/p$	hydraulic diameter
LS	leading side

Nu_0	Nusselt number computed with Dittus-Boelter correlation
Nu_s	Nusselt number for the static case of [12]
p	test section perimeter without ribs
R_x	radius of rotation
Re_{Dh}	Reynolds number
Ro	rotation parameter
T_b	bulk flow temperature
T_w	wall temperature
TS	trailing side
Tu	Turbulence intensity computed on u,v,w
$Tu_{xy'}$	Turbulence intensity computed on u,v’
u,v,v’,w	velocity fluctuations on x, y, y’, z directions
U_b	bulk flow velocity
U,V,V’,W	mean velocity components on x, y, y’, z directions
x,y,z	radial, peripheral and normal coordinates
y’	wall normal direction
Ω	rotational speed

1. INTRODUCTION

The study about the effects introduced by rotation on the thermal and flow fields inside internal cooling passages adopted in the rotor blades of gas turbines has recently seen a growing interest in the research community. Indeed, dedicated test rigs and experimental methodologies have been developed in the last years with the specific aim to investigate these complex flow and thermal fields. When a specific cooling passage is subjected to rotation, two are the main physical phenomena that can have an impact on the coolant path: the rise of Coriolis forces and the appearance of buoyancy effects [1, 2]. The former effect is usually characterized by the rotation parameter defined as $Ro=\Omega D_h/U_b$ and which takes into account the relative importance between peripheral velocity and bulk flow velocity. More precisely, the Coriolis acceleration ($a_c=-2\mathbf{\Omega}x\mathbf{C}$, where $\mathbf{C}$ is the relative velocity vector) that acts on the relative flow inside the duct causes the establishment of a spanwise pressure gradient that counterbalances its effects (Fig.1). If a confined flow with non-uniform velocity distribution is considered, a local unbalance between pressure gradient and Coriolis forces is found inside the regions of lower momentum fluid, hence a local flow deflection is induced and a secondary vortical flow establishes in the duct cross section, as sketched in Fig. 1. In the rather common case of a radial outward flow inside a rectangular channel in orthogonal rotation (i.e. with the rotation axis parallel to the duct height, the situation sketched in Fig. 1), the slower near wall flow is pushed towards the leading side (LS) of the duct by the Coriolis induced pressure gradient. Consequently, for continuity, the core fluid is displaced towards the trailing side (TS) of the duct and a symmetrical pair of vortex cells rises (Fig.1) [3].

The second main effect of rotation is described by the buoyancy parameter defined as:

$$Bo = Ro^2 \frac{R_x}{D_h} \frac{T_w - T_b}{T_b}$$

and which expresses the ratio between buoyancy forces and bulk flow inertial forces. The Bo parameter is proportional to Ro^2 and depends on the ratio between the local radial position (R_x) and the duct hydraulic diameter (D_h). The effect is triggered by a non-uniform fluid temperature, hence density, distribution that can be characterized by the temperature difference existing between the walls (T_w, usually hotter than the fluid) and the bulk flow (T_b). More precisely, the hotter (hence with lower density) near wall fluid experiences a lower centrifugal force than the colder (hence with higher density) core fluid. This, can alter substantially the flow topology and consequently the heat transfer field with respect to an isothermal situation ($T_w=T_b$).

The most recent contributions in literature that deepen the comprehension about these phenomena, with specific reference to gas turbine cooling channels, deal with the study of the interaction between rotation effects and those induced by the adoption of turbulence promoters on the channel walls [4].

Complex geometries have also been investigated, such as triangular [5], trapezoidal shaped [6, 7] and multipass channels with bends [8, 9]. For a simplified channel configuration (single-side rib-roughened rectangular channel with radial outward flow) Coletti et al. [4] showed that the separating/reattaching flow pattern promoted by the ribs is highly affected by rotation. In particular, if the background flow vorticity has the same orientation of the angular velocity of the rotating system (e.g. inside the boundary layer on the LS of a rectangular channel with radial outward flow) a stabilizing effect on the boundary layer is induced and a wider recirculation area is found downstream of the obstacles, vice versa occurs at the TS. If non-isothermal conditions are also considered [10], buoyancy effects cause an higher mixing in the near wall flow, with much higher effects on the stabilized side wall where the extension of the separated flow region is further increased, conversely less significant differences are found about the extension of the recirculating flow on the opposite wall.

In the case of rectangular or square channels in orthogonal rotation the basic description about the rotational effects reported above allows a rather good prediction about the main flow features that rise inside the passage. On the other hand, if more complex geometries are considered, the analysis is rather less trivial as shown by [6, 7] for a trapezoidal channel used for trailing edge cooling or in case of a triangular leading edge passage investigated in [5]. In particular, the latter contribution showed that inside a smooth triangular channel a non-symmetrical Coriolis vortices pair is found, with separation and reattachment points that are no longer located about the mid span of the lateral walls, but are instead located on the triangle upper apexes. Moreover, a steady flow configuration is never reached, indeed as the flow develops along the channel, more than two Coriolis vortical cells are found inside the channel cross section. The phenomenon is caused by a periodical reversal of the spanwise velocity component (i.e. the velocity component normal to both the rotation axis and the radial direction) inside the low momentum region found at the leading apex. The overall behaviour is strongly fastened if Ro is increased.

The present work is the first part of a research activity that aims at extending the previous findings about the rotational effects inside triangular shaped ducts by considering also the effects of turbulence promoters and by introducing buoyancy effects. Indeed, concerning leading edge cooling systems, the wide open literature provides an abundance of works focused on thermal investigations and rather complex geometries such as channels with curved walls [11] or systems where cooling is provided by means of jet impingement combined with coolant extraction [12]. Moreover, if rotating channels are considered, the availability of results is further reduced in regards of experimental works and flow field investigations.

For the reasons thoroughly explained in the previous discussion on rotation effects in cooling channels, since information available on simple geometries (i.e. rectangular channel) cannot straightforwardly apply to more complex ones (i.e. triangular channel), this work frames in the logic of understanding the main flow features inside triangular channels. The final goal is to create a background knowledge comparable to the already consolidated on rectangular channels [3, 4, 10] to deepen the comprehension of the thermal studies.

In order to fulfil this purpose, experiments have been conducted on the same rig used by Pascotto et al. [5] but on a modified test section that allows the heating of the lateral walls that have also been equipped with square orthogonal ribs. As in Pascotto et al. [5], the choice for this geometry (i.e. a single passage duct with an equilateral triangle cross section and without extraction holes for film cooling), beside the previous discussion, is motivated by the availability of a wide thermal analysis provided in [13, 14] and that can be complemented by the present findings.

2. TEST RIG AND EXPERIMENTAL METHODOLOGY

2.1 Test rig

The present experimental activity has been conducted on the facility of the Turbomachinery and Energy Systems Laboratory of the University of Udine. A detailed description of the rig can be found in [6]. The facility has been designed to allow detailed flow field investigations inside rotating ducts representative of modern cooling system for gas turbine blades and has been recently upgraded for thermal measurements as well. In particular the system has been provided with a rotary fluidic joint (Fig. 2(a)) equipped with 32 slip rings used for signal and electric power transmission on board of the rotating system.

The test section consists of a straight channel 820 mm long with an equilateral triangle cross section of side L=130 mm, (Fig. 2). Square ribs of height h=6.5 mm are placed perpendicularly to the channel main axis on the two lateral walls. The ribs have a pitch of 8h and have a staggered disposition with respect to the two channel sides, i.e. with the same geometrical characteristics as in [13, 14]. In order to investigate buoyancy effects, each ribbed wall has been machined out of a single aluminium slab. Heating is provided by powering with direct current a 25 μm thick Inconel sheet attached on the external surface of the wall (Fig. 2(e)). An external layer of insulating material minimizes the thermal losses towards the environment. The temperature of each heated wall is monitored with four thermocouples installed inside the aluminium walls (Figs. 2(c, e)) in the inter-rib regions just upstream and downstream the investigated area (planes yz and xy' in Figs. 2(c, d)). The calibration of the temperature sensor (connected to the slip rings) and a data averaging process computed on stencils of 20 samples acquired at 2 Hz lead to an overall uncertainty of ±0.75 K. Hot test conditions have been obtained by heating the ribbed walls up to 110 °C. Differences of 1K have been observed between the readings of two thermocouples placed on similar points of the same wall but in the two different inter-rib locations, while the maximum difference between the hottest and the coldest readings was equal to 5 K and has been observed for tests at the highest rotational speed.

The test section is fed with air at ambient conditions through a rotating settling chamber connected to the rotary fluidic joint. The settling chamber design (Fig. 2(a)) is such that a uniform flow distribution is ensured at the duct inlet, where a 40mm long honeycomb filter prevents also from flow separation. At the channel outlet, the exhausted flow is collected in a small settling chamber and then leaves the test section through a return passage, so avoiding any flow perturbation near the tip region that could conversely occur under rotation if a free radial outlet was set. The return channel was also adopted by [13, 14], but in their case it was necessary in order to pressurize the channel and, therefore, to reach very high rotation numbers.

All tests were performed with the channel z axis aligned with the angular velocity, as depicted in Fig. 2. The test section was spun in both sense of rotation, in order to investigate the flow field on both leading and trailing sides of the channel without changing the PIV measurement set up (see next section).

2.2 Flow field measurement methodology

Flow field measurements were performed by means of 2D and Stereo-PIV techniques. A single camera configuration (Fig. 3(a)) for 2D measurements was used on plane xy' (Fig. 2(d)), while a double camera configuration (Fig. 3(b)) for Stereo-PIV measurements was used on plane yz (Fig. 2(c)). The PIV system is custom-made and was already described in [7].

The PIV raw data (PIV image pairs) were processed using the commercial software PIVview (from PIVTEC Gmbh). In particular, for the Stereo-PIV data, image back-projection and then stereo reconstruction were performed; furthermore, a disparity correction was also used in order to minimize the misalignment errors [15]. Stereo calibration of the measurement chain was achieved inside the channel by means of multiple images of a target placed at first on the image plane and then displaced in six adjunctive off-plane positions. The nominal magnification of the PIV images ranges from 17 pixel/mm (Stereo-PIV) to 20 pixel/mm (2D-PIV), which turns in a vector resolution from 1.06 to 1.25 vectors/mm, respectively.

As can be seen from Fig. 3, the present PIV system is fixed, i.e. not rotating with the test section. Consequently, the measurements at Ro>0 are carried out in phase-locked mode and, therefore, the direct output of the PIV raw data is the absolute flow field. The relative field inside the test section is obtained by subtracting the local peripheral displacement of the system from the PIV data with an ad-hoc procedure. For the case of PIV measurements conducted on flow planes perpendicular to the rotation axis, Armellini et. al [16] proposed a specific pre-processing methodology to be applied to the PIV raw data (image pairs) and that allows to keep the peripheral displacement subtraction error below 1%, i.e. allows to provide a final accuracy level close to the one of standard 2D measurements on static test sections. Unfortunately, the aforementioned methodology cannot be directly used for the present case because the selected measurement planes are not perpendicular to the rotation axis (see position of plane xy' in Figs. 2(d), 3(a) and 4). Indeed, since a component of the peripheral displacement lies on the out-of-plane direction (Fig. 4), a correct image reconstruction would need a precise knowledge of the perspective view realized by the optical system, resulting in a rather complex implementation of the methodology. In view of this, a different approach has been chosen, namely the second exposure of each PIV image pair has been pre-processed by applying a rigid translation of the image in order to reduce the walls' displacement at less than 1 pixel with respect to the first exposure. This raw peripheral displacement subtraction allows the PIV image processing algorithm to resolve particle displacements of standard magnitude (±10 pixel) and to impose the correct boundary conditions on the processing mesh (i.e. no-slip condition at the solid walls). Successively, the displacement components applied for the rigid image translation are added to the resulting data in order to restore the absolute velocity field. The post-processing procedure is then completed by the subtraction of the real peripheral velocity field (the in plane component in Fig. 4), which is accurately measured as described at the end of this section.

The processing of the 2D data is further complicated by the need to compensate for the parallax error associated to the out-of-plane component of the peripheral displacement (plane xy' is not perpendicular to the rotation axis, see Figs. 2(d), 3(a) and 4). More in detail, even if rather long focal lenses have been used, it is not possible to assume that the light is collected with parallel rays. Consequently, the out of plane component of the peripheral displacement will be seen by the camera as an additional in plane displacement (i.e. the parallax error) which magnitude and orientation is proportional to the distance between a specific measurement point and the intersection of the camera optical axis with the measurement plane (Fig. 4). Therefore, the peripheral displacement recorded by the camera, is different from the real in plane one (which can be calculated as $v = \Omega R\cos(\alpha)\Delta t$, where R is the radial position, Ω is the measured angular velocity and Δt is the PIV separation time). For the present data on plane xy', the maximum magnitude of the out-of-plane peripheral displacement was

14 pixel, hence the resulting in-plane parallax component can be up to 0.9 pixel, which is a not negligible value. A precise parallax error compensation requires the knowledge of two main input data: the lenses focal length and the position of the optical axis projection on the image plane. For sake of accuracy, the actual value of the lens focal length has been directly measured with a dedicated procedure (i.e. to measure the size of the field of view framed with the present optical configuration) and turned out to be equal to 108.5 mm.

Optical axis projection position has been determined by an in-situ calibration realized with a target that allows to frame straight lines aligned with the out-of-plane direction on planes either parallel (Fig. 5(a)) or perpendicular (Fig. 5(b)) to the channel wall. An iterative procedure is carried out by moving the target until the lines drawn on its surface are seen as points by the camera (procedure exemplified in figures 5(a, b)), hence defining position of the projection of the camera optical axis on the image plane. Examples of parallax error compensation displacement fields are reported in Figs. 5(c, d) for the case Ro=0.6. As can be seen, the projection of the lenses optical axis (highlighted by the intersection of the two red lines in figures 5(c, d)) has been placed close to the area where flow recirculation is supposed to be found. This choice guarantees that the most critical area of the analysed flow field is only marginally affected by the parallax error and by the possible uncertainties of its compensation. It is worth to mention that the parallax correction has to be applied to the 2D measurements only, since the Stereo 3D measurements are parallax free by definition.

The determination of the peripheral displacement field requires to know the real position of the measurement points with respect to the rotation axis, the test section angular velocity, and to ensure a reliable synchronization of the PIV system with the test section angular position. Concerning the centre of rotation position evaluation, a two steps indirect methodology has been used. As a first step, the procedure proposed in Armellini et al. [16] is followed, namely a target with a rectangular grid of dots is placed inside the test section on plane z=0 and it is framed by an auxiliary camera with optical axis parallel to the axis of rotation (aux camera in Fig. 3(a)). Two exposures of the target are taken with the test section at two angular positions. The markers centre positions are determined in the two images by means of a cross-correlation with a sample signal and afterwards, the centre of rotation position can be determined applying a least square method on the markers displacement. Providing that the number of dots is sufficiently large, the centre of rotation with respect to a reference point of the target can be located with an accuracy of ±0.1 mm. The second step requires to operate the laser and to acquire an image of the laser sheet trace on the calibrated target. The analysis of this realization allows to get an accurate determination of the position of the laser sheet trace with respect to the centre of rotation.

The last technical issues that have to be addressed are the synchronization of the PIV system with the test section rotation and the measurement of the actual peripheral velocity. Both these issues are solved by sampling the TTL signal from a photodiode (see Fig. 3(b)) periodically screened by the test section, all the technical details can be found in Armellini et al. [6]. The mean angular velocity for each revolution, Ω, can be computed with a relative error equal to $\delta\Omega/\Omega=3.5\text{x}10^{-7}$, while image positioning stability is kept by far smaller than the data spatial resolution (i.e. with image shifts about ±1 pixel), so reducing to negligible values the spatial averaging error.

2.3 Uncertainty analysis

Concerning PIV data accuracy, only statistical flow quantities will be presented, resulting from the ensemble average of 10^3 instantaneous samples. For a static 2D measurement, the overall upper bound estimate of the mean velocities uncertainty results to be less than 2% with respect to U_b (95% confidence level), while the maximum uncertainty in the estimate of the higher order statistics is 5% of U_b. For the data acquired under rotation, the pre- and post-processing procedures used for the peripheral displacement field subtraction introduce further unavoidable error sources that increase the overall uncertainty on the mean velocities up to 5% of U_b. A proof of the reliability of this estimation is provided by Fig. 6, where a cross comparison between 2D and Stereo-PIV data is provided for the most critical case of Ro=0.6. The plots clearly show a rather good superimposition of the data with maximum differences of about $0.05U_b$.

2.4 Test conditions

All tests have been conducted at $Re_{Dh}=10^4$ defined on the duct hydraulic diameter (D_h = 75.05 mm), on the flow bulk velocity (U_b=2.1 m/s), and flow properties measured at the inlet of the test section (see $T_{air,in}$ in Fig. 2(c)). Rotation numbers of 0.2 and 0.6 have been reached by spinning the test section at about 55 and 160 rpm, respectively. Ribbed walls temperatures of about 110°C corresponded to Bo=0.08 and 0.7 for the two rotating conditions of Ro=0.2 and 0.6, respectively. The given Bo values are computed at the radial position where the measurement plane yz is found (R_x=709 mm, Fig. 2(c)). The present working conditions are considered to be representative of current engine conditions and have been selected in order to be consistent with the available studies [5, 13, 14].

For computation of Bo, averaged values of both wall and bulk fluid temperatures have used, namely the average of the 8 thermocouples installed inside the aluminium walls for T_w, and the average between $T_{air,in}$ and $T_{air,out}$ for T_b. In view of the unavoidable measurement errors and the slightly non-uniform temperature distribution of the walls previously commented, an uncertainty of ±5% has to be considered for the present definition of Bo. Concerning the computation of Re_{Dh} and Ro values, the main error source comes from the measurement of the air flow rate that causes a final uncertainty of about ±1.5%.

3. RESULTS

3.1 2D data on plane xy'

The characterization of the separation structure downstream of the ribs is obtained by the data acquired on plane xy', i.e. the plane perpendicular to both the channel wall and the rib axis (Fig. 2(d)). Figure 7 reports the reference conditions measured for the static case. The time-averaged stream tracers' path depicts a separation structure that extends up to about x/h=3.5 and a corner vortex located on the upstream face of the following obstacle. Contour plots of the in-plane turbulence intensity, $T_{xy} = \frac{1}{U_b}\sqrt[2]{\frac{u'^2+v'^2}{2}}$, are reported in Fig. 7(b) (the withe areas that surrounds the ribs and close to the bottom wall are zones of non valid data, which quality has been spoiled by unavoidable laser light reflection). As expected, the detected flow features are in agreement with those observed in a rectangular ribbed channel [17].

A summary of the results obtained under rotation is reported in Figs. 8 and 9 in terms of stream tracers path and Tu_{xy} levels, respectively (again, blanked regions are not valid data). When the investigated wall is at the TS (Fig. 8(e-h)), no remarkable effects of both rotation and buoyancy are observed on the flow topology, with the only exception of a small reduction of the recirculation extension found for Ro=0.6. Similar observations are reported also in [10] for the case of a rectangular duct in orthogonal rotation. The explanation of this behaviour is linked to the destabilizing effect that rotation has on the separation structure at the TS, which causes rather strong flow turbulence that reduces the bubble extension and mitigates local density gradients. Also in the present case, higher Tu_{xy} are measured at the TS (Fig. 9(e-h)) with respect to both static case (Fig. 7(b)) and LS (Fig. 9(a-d)). More in detail, the Tu_{xy} level increases with Ro, and this effect is enhanced by buoyancy.

On the LS, the behaviour is different depending by the Ro value. At Ro=0.2 (Fig. 8(a, b)), the separation bubble appears longer than the static case (Fig. 7(a)), in agreement with the stabilizing effect commented in [10]. Conversely, only marginal buoyancy effects are detected on both flow path and Tu_{xy} levels (Fig. 9(a, b)). This is also evident by the profiles of <uv'> extracted at y'/h=0.5 (see Fig. 2(e)) and reported in Fig. 10(a). Indeed, the comparison of heated/non-heated cases reveals almost identical behaviours, while the destabilizing/stabilizing effects are rather clear as demonstrated by the higher values and peaks closer to the obstacle found for TS cases. A different behaviour is found at Ro=0.6 (Fig. 8(c, d)), where the separation bubble gets only marginally longer with respect to the static case (Fig. 7(a)) and, unexpectedly, the flow agitation is higher for the non-heated case than the heated one (Figs. 9(c, d) and 10(b)). Nevertheless, this turned out to be only a local feature, as it will be clarified later on with the plot of Fig. 14. Finally, it is also worth to observe that the stream tracers inside the recirculation regions at the LS show a pronounced centripetal path that is an indication of a relevant 3D character of the flow. This evidence could be at the basis of a possible explanation of the differences commented about the present flow behaviour with respect to the one found for a rectangular channel [10]. This issue is further discussed in the next section.

3.3 3D data on plane yz

Stereo-PIV measurements in plane yz, located at 495 mm from the inlet section (downstream the honeycomb filter, or 709 mm from the rotation axis, see Fig. 2(c)), have been conducted in order to characterize the rotational effects on the overall flow structure. In order to ease the present data analysis, Fig. 11 reports the results found for the smooth, non heated channel configuration obtained on the same rig and reported in [5]. The Coriolis induced secondary flow is characterized by a vortex pair at the lowest rotation condition (see vortices A and B in Fig. 11(a)) and shows a remarkable sensitivity to the change of Ro. Indeed, at Ro=0.4, a third vortex (B2 in Fig. 11(b)) appears close to the LS apex, producing a rather more complex flow distribution. Pascotto et al. [5] provided a justification of this behaviour and shown how it grows in its complexity as rotation is further increased. Moreover, the streamwise velocity distribution turned out to be strongly asymmetric, with higher magnitudes on the TS and a pronounced peak located near the lower apex (Fig 11(c, d)). These features were associated to the channel thermal behaviour reported in [13].

The secondary flow distribution measured inside the ribbed duct is reported in the plots of Fig. 12. A comparison with the smooth channel case of Fig. 11(a) can be made by looking at the data with the same sense of rotation (i.e. with the LS on the left, Figs. 12(a)-(d)). With respect to the smooth case, the clockwise vortex previously found close to the lower apex of the duct (vortex B in Fig. 11(a)) is now rather bigger and extends almost over all the channel cross section (B in Fig. 12(a)). The counter-clockwise vortex (A in Fig. 12(a)) is confined close to the upper, non ribbed wall and appears to be too small to be well captured at the present data resolution. Moreover, the local flow acceleration on top of the rib (which region is bounded by the 3D separation line that extends all along the rib span at the TS, see Fig 12(a)) pushes the rotation induced vortices closer to the LS, causing an evident flow deviation towards the upper wall in the inter rib region at the LS. This is in agreement with the previous observation about the 3D nature of the separation found behind the obstacle (see comments about Figs. 8(a-d)). Finally, if cases at different Ro are compared (see Figs. 12(a) and (c)) the sensitivity of the flow topology on plane yz to the change of Ro is practically absent. Moreover, if heated and non heated cases are compared, no clear effects of the buoyancy are found (see Figs. 12(b, d) and (a, c)). More evident differences can be instead appreciated in the contour plots of the U velocity component reported in Figs. 13(a-d) (blanked areas on top of the rib are regions of not available data due to optical accessibility). Indeed, as Ro and Bo are increased, higher velocity peaks are found at the TS as a consequence of the stronger Coriolis induced secondary structures produced at higher rotation. The absolute velocity peak on the lower apex that characterize the flow field inside the smooth channel (Fig. 11(c-d) is instead no longer detected.

If the test section is spun in the opposite sense of rotation (Figs. 12(e-h) and 13(e-h)), the Coriolis induced vortex B is correctly found on the right of the plots and with counter-clockwise rotation, i.e. close to the LS and pushing core flow toward the TS. Vortex A is again smaller in size and remains confined close to the upper, non ribbed wall. With respect to the previous comments, the main differences concern the features of the flow in the inter-rib region at the TS that, conversely to what happens at the LS, is by far less 3D (Figs. 12(e-h)) and is characterized by a more uniform U velocity distribution (Figs. 13(e-h)). Again, slight effects caused by an increase of Ro and Bo are found only in the U velocity peaks found close to the TS (Figs. 13(e-h)).

A final comment about the effect of rotation and buoyancy can be made by looking at the Tu contour plots of Fig. 14. The stabilizing/destabilizing effect of rotation can be appreciated by comparing the Tu levels between leading and trailing sides at the same working conditions (compare frame (a) and (c) or (b) and (d)), with higher values always observed at the TS. Similarly, the stronger flow mixing promoted by buoyancy is associated to the overall higher Tu levels measured for the heated cases (compare frame (a) and (b) or (c) and (d)). This in not in contrast with the comments about Fig. 10(b). Indeed also in Fig. 14(b), at the position of plane xy’ (see Fig. 2(d)) the Tu values for Bo=0.7 are smaller than those for non-heated case in Fig. 14(a). Therefore, the commented behaviour about the separated flow length and agitation level at the LS, that differ substantially with respect to the rectangular channel case [10], as to be ascribed to local flow effects that are peculiar of the triangular geometry, demonstrating once more the need for dedicated analysis.

4. THERMAL EFFECTS

After providing a description of the time-averaged flow features developing inside the rotating channel, a further discussion can be addressed concerning the combined effects of rotation and buoyancy on the thermal performances of the device. This is possible by exploiting the available data from [14]. Figure 15 reports the thermal data from [14] for a set of flow conditions that are comparable to those considered in the present work, including also the values at Ro=0. The plots show the distributions of the Nusselt number enhancement, Nu/Nu_0 and Nu/Nu_s, along the channel length and for variable flow conditions. The Nu is the result of wall temperature measurements performed in the experiments while Nu_0 is the one obtained from the Dittus-Boelter correlation and Nu_s refers to the static channel case. In Fig. 15, L1/T1 refer to the half portion of the leading/trailing sides close to the bottom apex, while L2/T2 pertain to the upper half of the leading/trailing sides close to the upper apexes. The following analysis will be based only on the 3D data on plane yz, since plane xy' is located just in between of the L1/L2 or T1/T2 zones defined in [14].

At first, Figs. 15(a, b) show that rotation sets a substantial increment of Nusselt number in zone T2. The regions adjacent to the lower apex, L1 and T1, experience also stronger heat transfer although limited with respect to the upper portion of the TS (i.e. T2). Conversely, zone L2 shows no increment or even less Nusselt values with respect to the stationary case. The present aerodynamic data can help to understand this behaviour. The plots in Figs. 12 and 13 show how the L2 region is permanently swept by the low momentum Coriolis vortex cell, while the adjacent velocity peak favours heat transfer in region T2. These flow features determine a velocity deficit near the L2 region, hence a heat transfer deficit with respect the whole channel section and a reduction with respect to the static case.

This flow behaviour, as previously commented in section 3.3, becomes even stronger if the Ro increases, and consistently does the enhancement factor from [14] (compare data in Fig. 15(a)-higher

Ro, with those in Fig. 15(b)-lower Ro).

Concerning the Bo effects, [14] shows an overall positive effect, with the highest increment of heat transfer again located in region T2, Fig. 15(c). Indeed, as demonstrated by the present data, the effect of buoyancy is an overall augmentation of the turbulent agitation of the flow (Fig. 14), in particular on the TS. On the contrary, in region L2 this effect is much less pronounced and the turbulent quantities remains practically unchanged at varying the Bo, consistently with the existence of the low momentum Coriolis vortex cell above commented.

CONCLUSIONS

Thanks to the present study, important conclusions are drawn about the buoyancy effects on the flow field inside a ribbed triangular channel. The main findings are summarized in the following.

- Buoyancy forces have only marginal effects that result in increased velocity peaks and in an overall enhancement of the flow agitation level. No remarkable modifications are found on the rotation induced secondary flows and on the separation downstream the ribs. This behaviour differs from the results in [10] for a rectangular channel, where buoyancy lead to a dramatic increase of the separation length behind the ribs at the LS.
- On the duct cross section, rotation induced secondary flows turned out to be strongly asymmetric and characterized by a single main vortex. Consequently, the present inter-rib flow is characterized by a condition by far different from the one realized in the region of pairing of two symmetric vortices that has been investigated by [10] in a rectangular ribbed duct. It is in the authors' opinion that this evidence is at the basis of the differences here commented.

The present analysis once more confirms the complexity of the flow topology inside this kind of devices, evidence that was already discussed for the smooth case [5]. Therefore, a precise explanation of the aero-thermal behaviour cannot be based on a simplified conjectured flow model but there is the need for a deeper understanding. Indeed, the present aerodynamic data allow a precise justification for the heat transfer performances in rotation that are available in the literature on the same geometry.

ACKNOWLEDGEMENTS

This work has been supported by the Italian Ministry of University and Research (MiUR).

REFERENCES

[1] Johnston J. P., Halleen R. P., Lezius D. K. (1972) *Effects of spanwise rotation on the structure of two-dimensional fully developed turbulent channel flow* J. Fluid Mech. 56, pp. 533–557.

[2] Morris W. D., Ayhan T. (1979) *Observation on the influence of rotation on heat transfer in the coolant channel of gas turbine rotor blade*, Proc. Inst. Mech. Engrs. 193, pp. 303–311.

[3] Speziale, C. G., Thangam S. (1983) *Numerical Study of Secondary Flows and Roll-Cell Instabilities in Rotating Channel Flow*, J. Fluid. Mech., 130, pp. 377–395.

[4] Coletti F., Maurer T., Arts T., Di Sante A., (2012) *Flow field investigation in rotating rib-roughened channel by means of particle image velocimetry*, Exp. Fluids 52, pp. 1043–1061.

[5] Pascotto M., Armellini A., Mucignat C., Casarsa L. (2014) *Coriolis Effects on the Flow Field Inside a Rotating Triangular Channel for Leading Edge Cooling*, ASME J. Turbomach., 136(3), p.031019.

[6] Armellini A., Mucignat C., Casarsa L. (2011) *Flow field analysis inside a gas turbine trailing edge cooling channel under static and rotating conditions*, Int. J. Heat Fluid Flow 32, pp. 1147–1159.

[7] Mucignat C., Armellini A., Casarsa L., (2013) *Flow field analysis inside a gas turbine trailing edge cooling channel under static and rotating conditions: Effect of ribs*, Int. J. Heat Fluid Flow 42, pp. 236–250.

[8] Elfert, M., Schroll, M., Förster, W.(2012) *PIV measurement of secondary flow in a rotating two-pass cooling system with an improved sequencer technique*, Journal of Turbomachinery, 134 (3), art. no. 031001.

[9] Lei, J., Li, S.-J., Han, J.-C., Zhang, L., Moon, H.-K. (2014) *Effect of a turning vane on heat transfer in rotating multipass rectangular smooth channel*, Journal of Thermophysics and Heat Transfer, 28 (3), pp. 417-427.

[10] Coletti F., Lo Jacono D., Cresci I., Arts T., (2014) *Turbulent flow in rib-roughened channel under the effect of Coriolis and rotational buoyancy forces*, Physics of Fluids 26, p. 045111.

[11] Domaschke N., von Wolfersdorf J., Semmler K., (2012) *Heat Transfer and Pressure Drop Measurements in a Rib Roughened Leading Edge Cooling Channel*, Journal of Turbomachinery, 134, art. no. 061006

[12] Andrei L., Carcasci C., Da Soghe R., Facchini B., Maiuolo F., Tarchi L., Zecchi S., (2013) *Heat transfer measurements in a leading edge geometry with racetrack holes and film cooling extraction*, Journal of Turbomachinery, 135 (3), art. no. 031020

[13] Liu Y.H., Huh M., Rhee D.H., Han J.C., Moon H.K.K. (2009)*Heat Transfer in Leading Edge, Triangular Shaped Cooling Channels With Angled Ribs Under High Rotation Numbers*, ASME J. Turbomach., 131(4), p. 041017.

[14] Liu Y.H., Huh M., Han J.C., Moon, H.K. (2010) *High Rotation Number Effect on Heat Transfer in a Triangular Channel With 45 deg, Inverted 45 deg, and 90 deg Ribs*, ASME J. Heat Trans., 132(7), p. 071702.

[15] Willert, C.(1997), *Stereoscopic Digital Particle Image Velocimetry for Applicationin Wind Tunnel Flows,"* Meas. Sci. and Technol., 8, pp. 1465–1497

[16] Armellini, A., Mucignat C., Casarsa L., Giannattasio P., (2012) *Flow field investigations in rotating facilities by means of stationary PIV systems*, Meas. Sci. Technol. 23, p.025302 (11pp).

[17] Rau, G., Moeller, D., Cakan, M., Arts, T., (1998) *The effect of periodic ribs on the local aerodynamic and heat transfer performance of a straight cooling channel*, ASME J. of Turbomachinery, 120, pp 368-375.

Figure 1

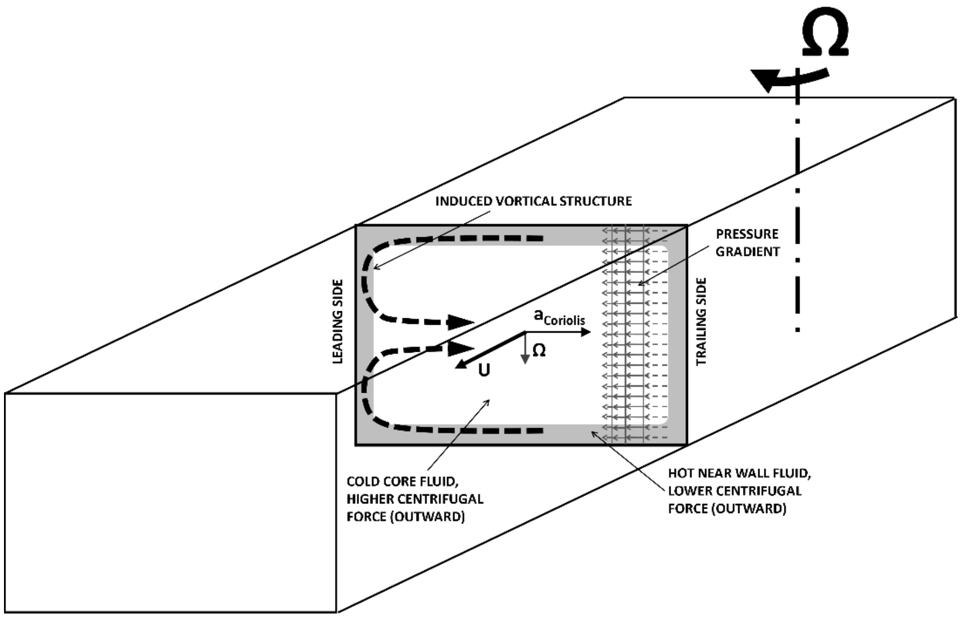

Figure 2

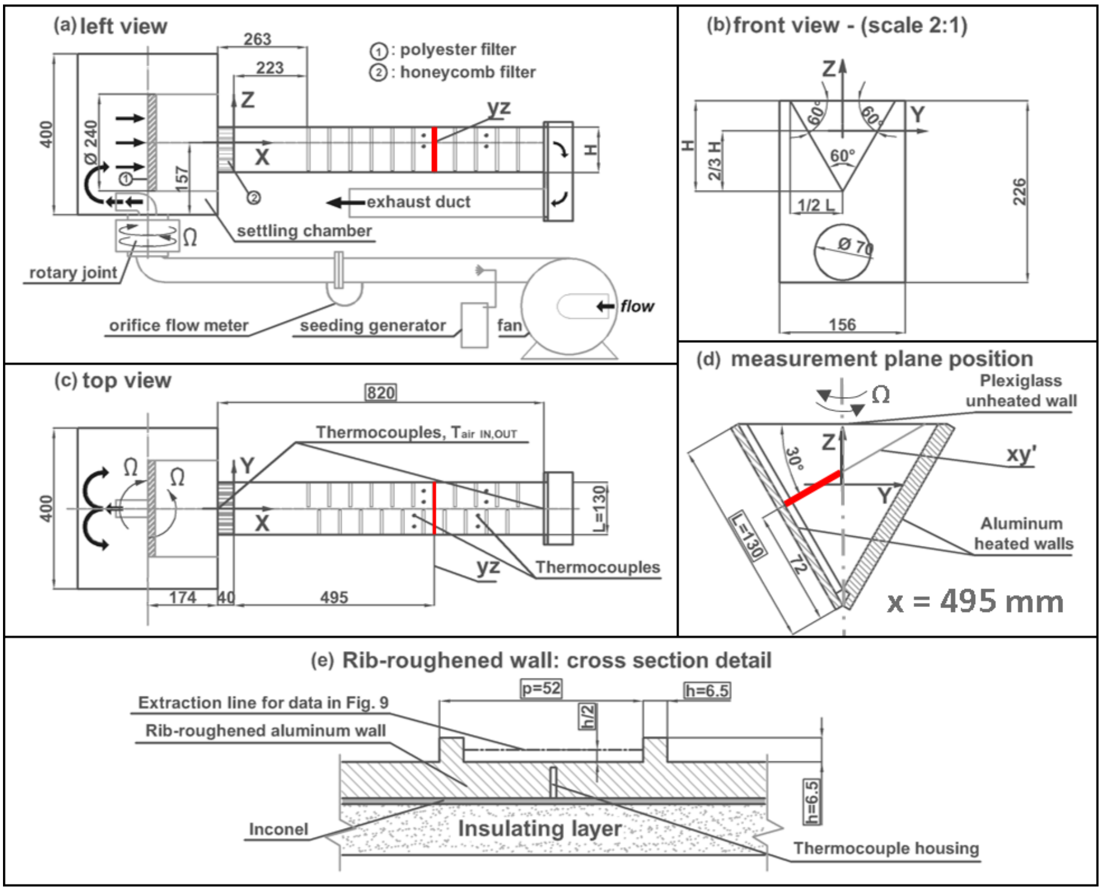

Figure 3

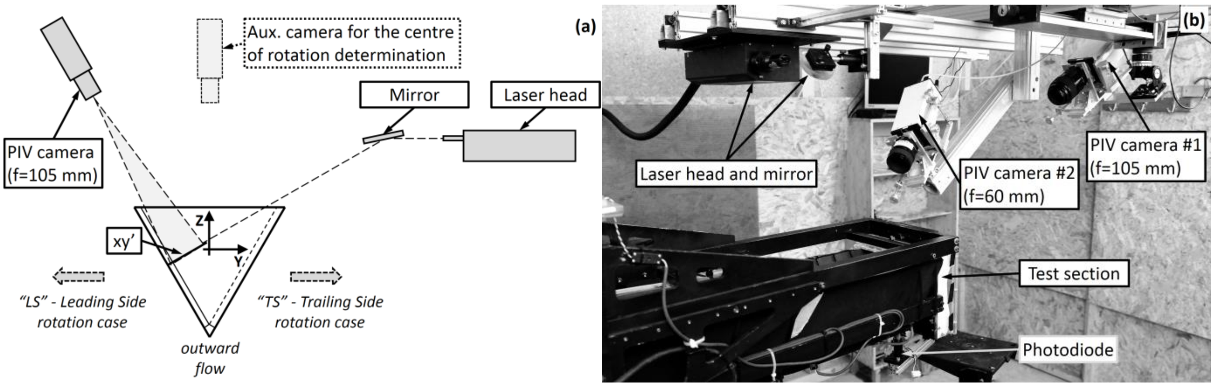

Figure 4

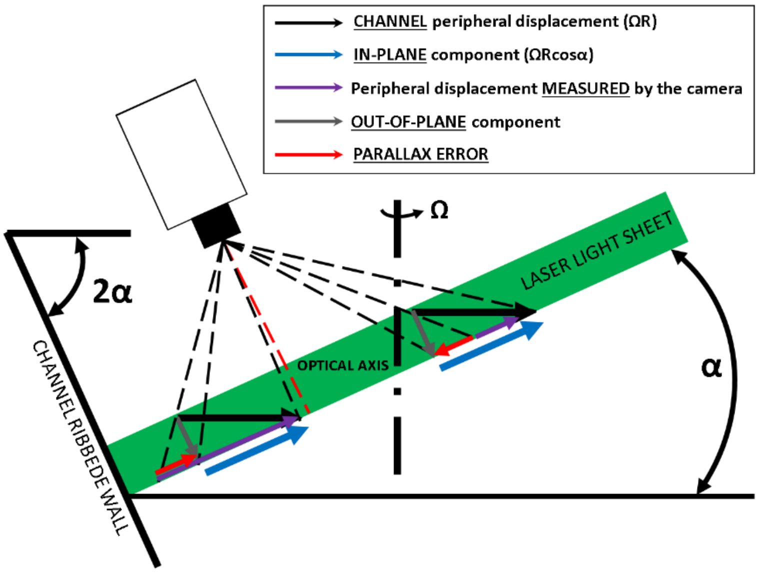

Figure 5

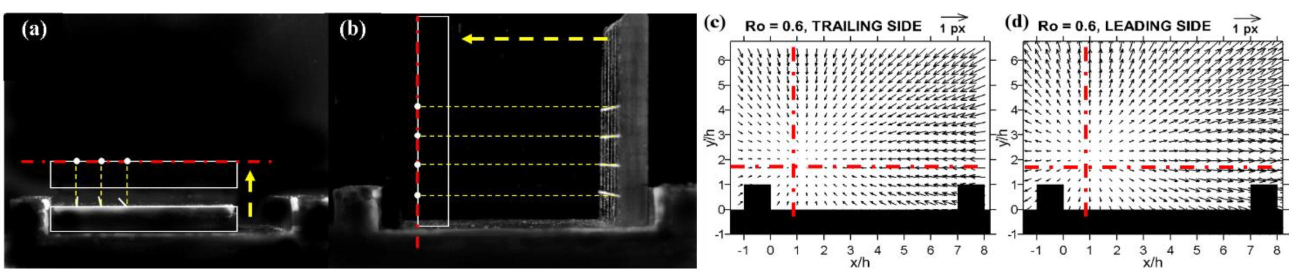

Figure 6

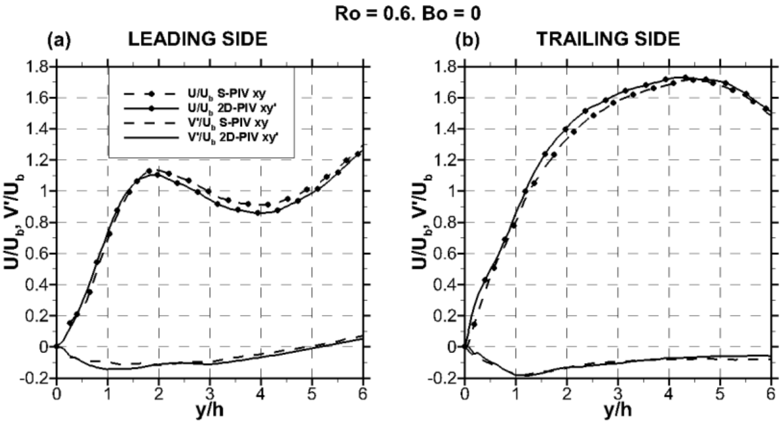

Figure 7

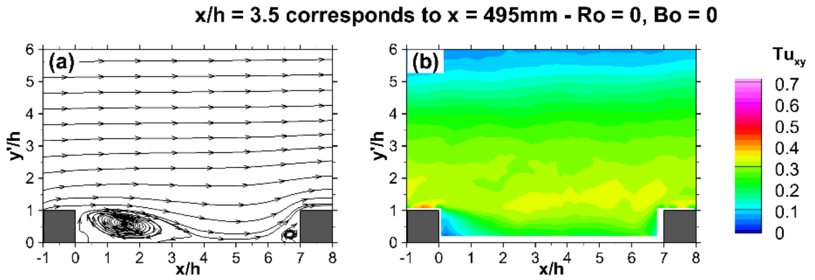

Figure 8

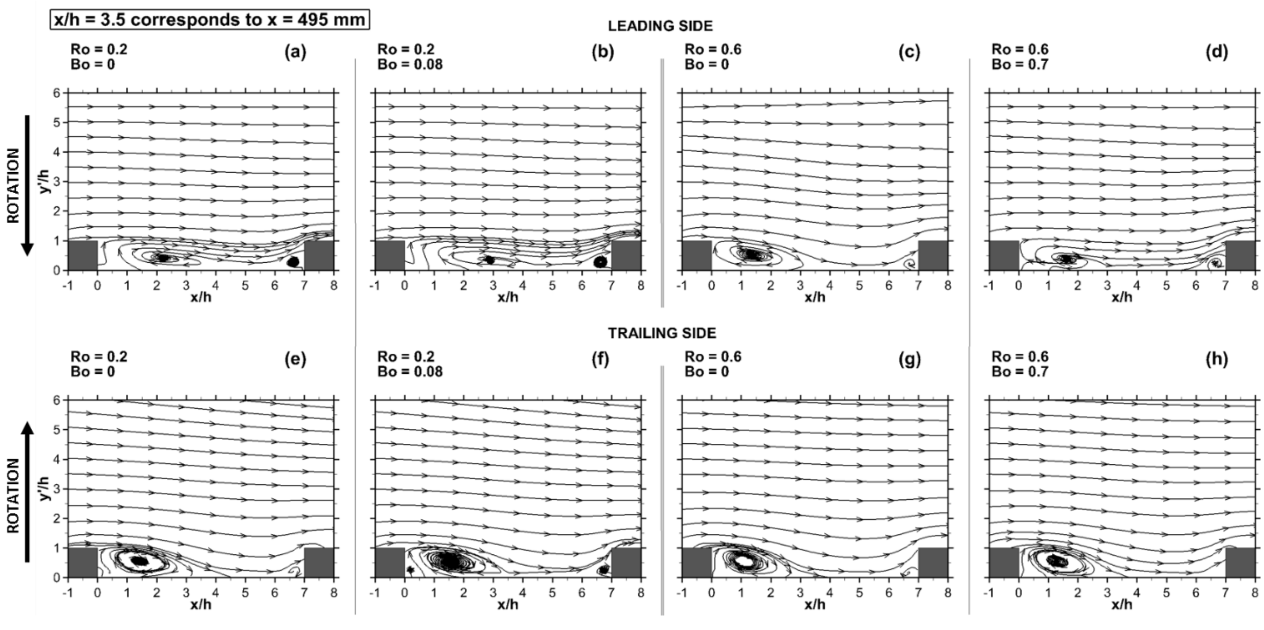

459

Figure 9

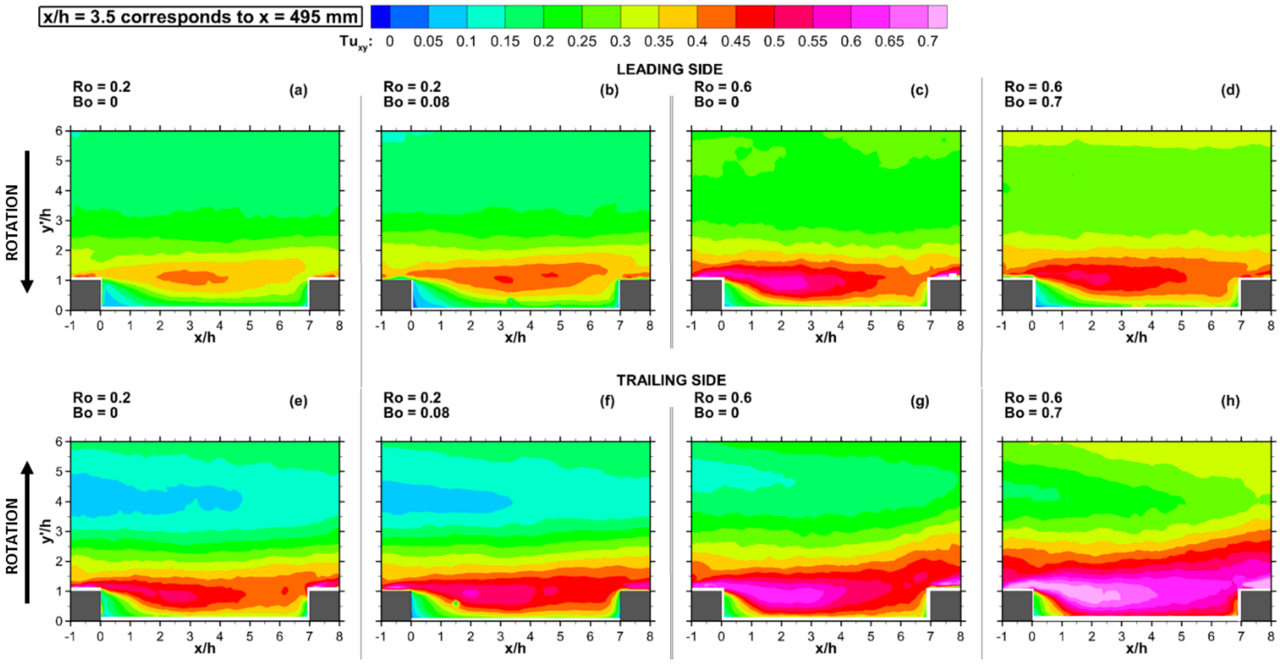

Figure 10

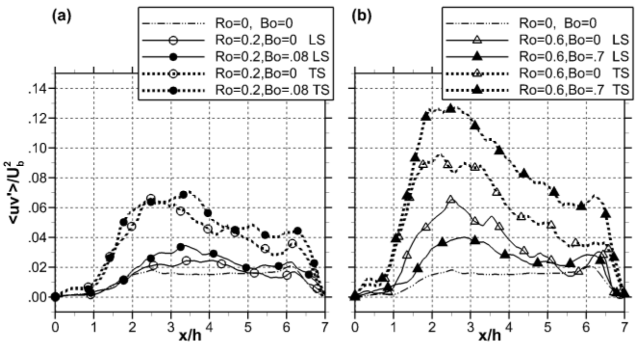

Figure 11

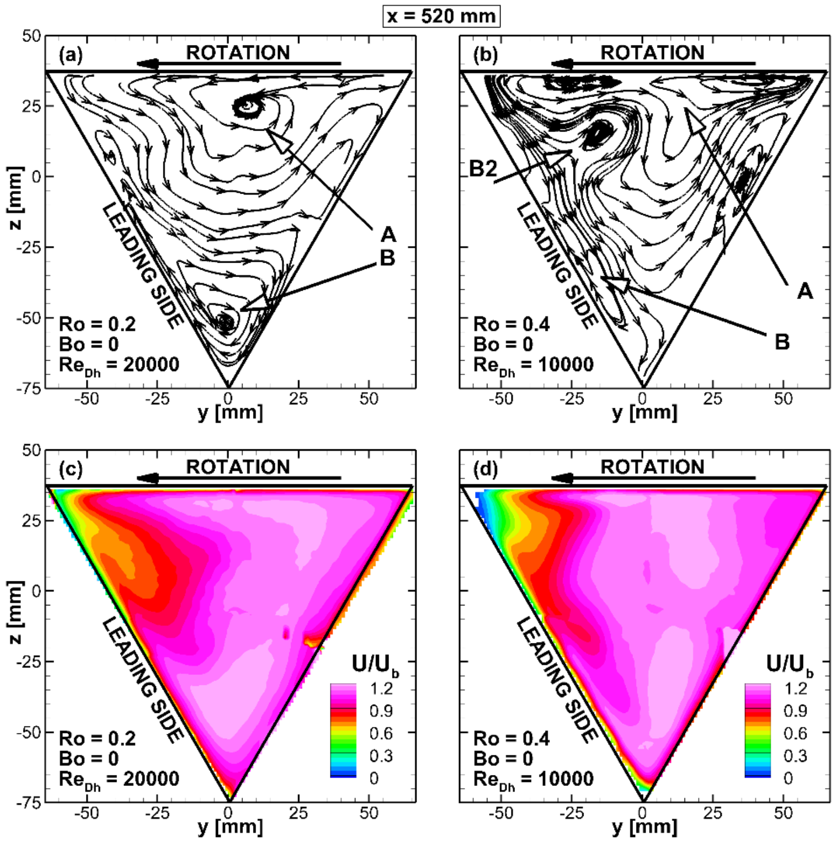

Figure 12

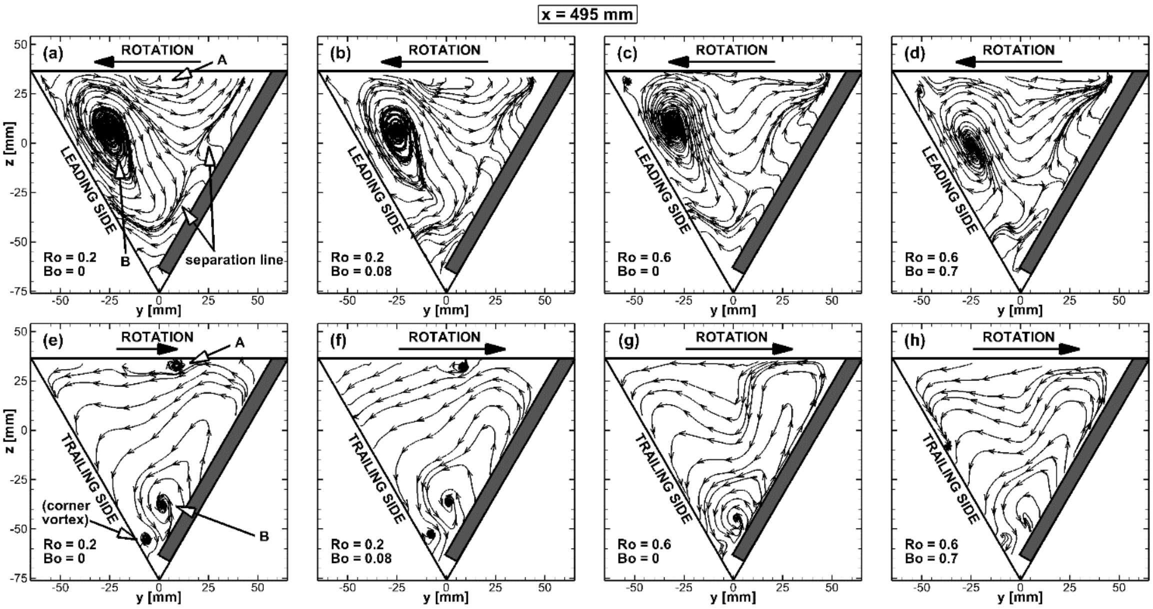

Figure 13

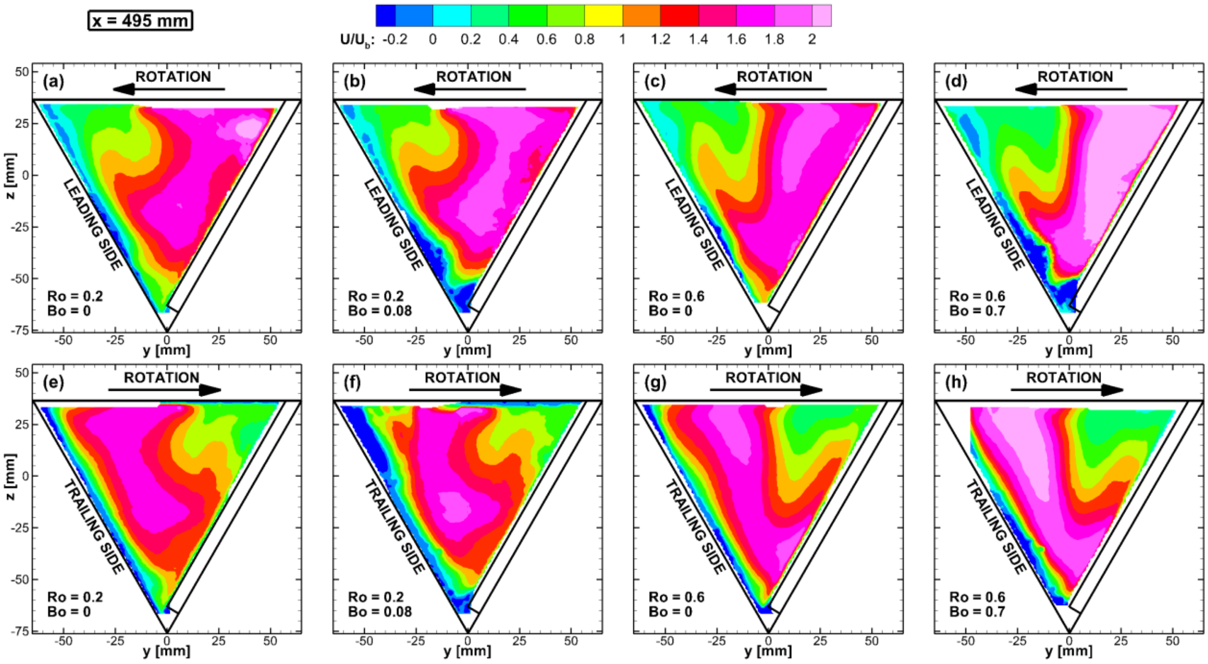

Figure 14

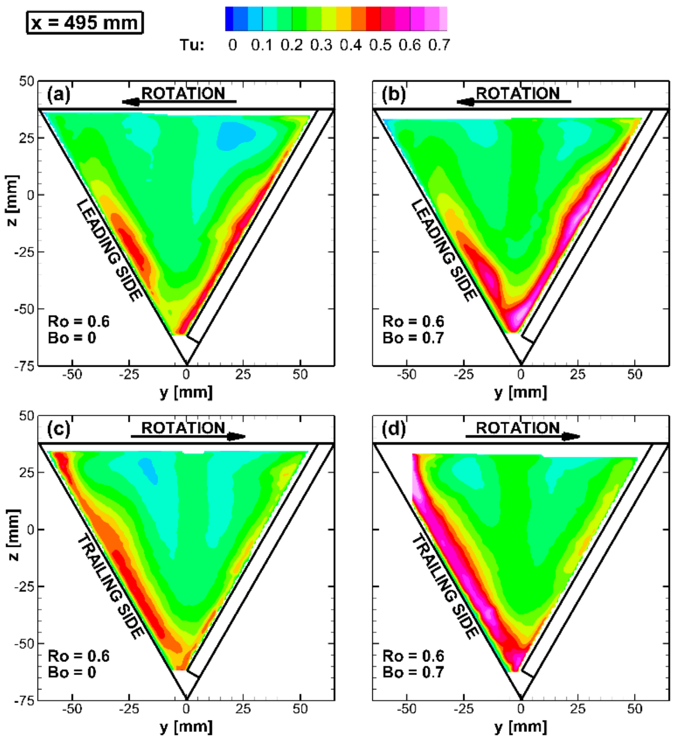

462

Figure 15

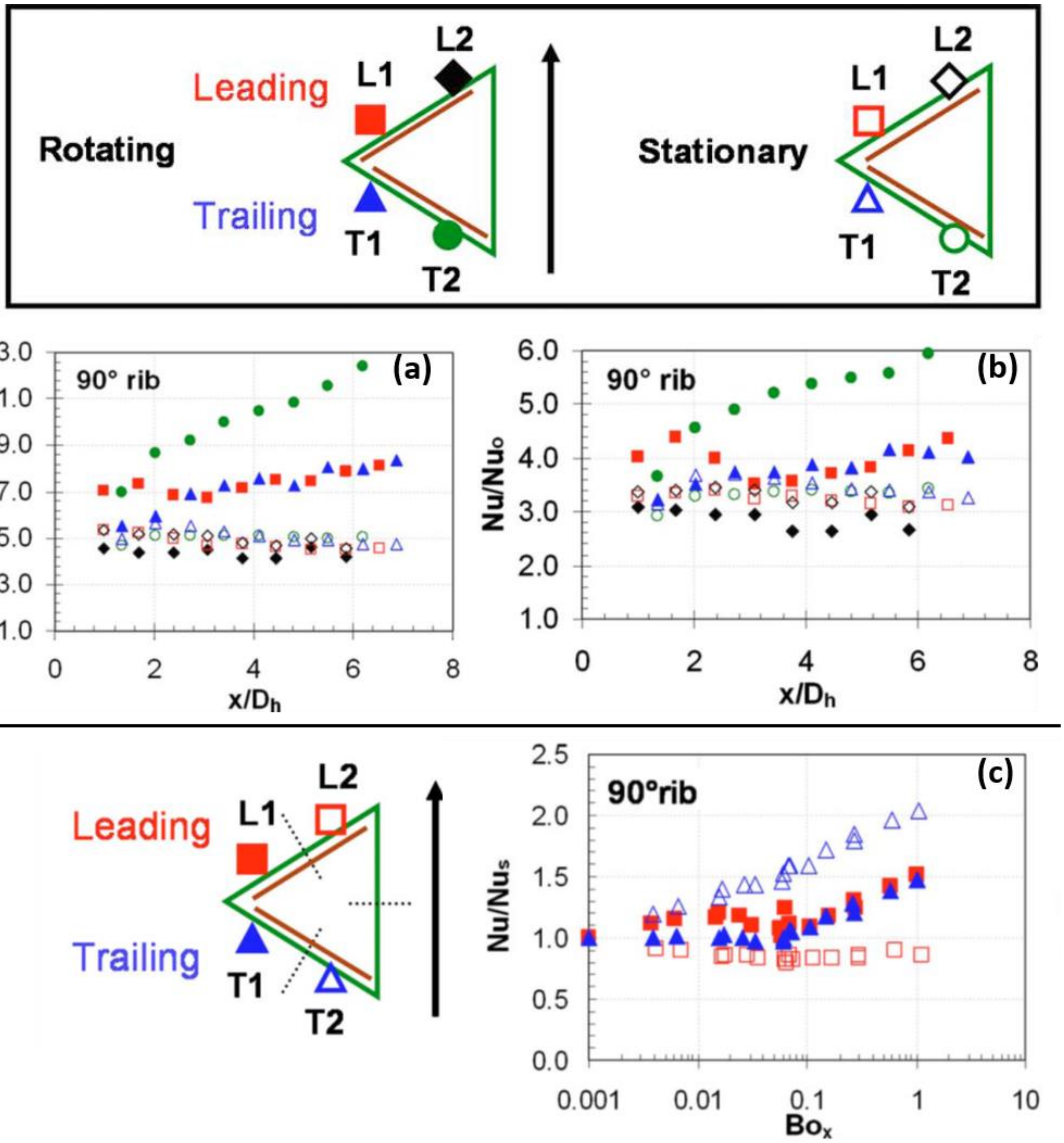
Rotating
Leading
Trailing
L1
L2
T1
T2
Stationary
90° rib
(a)
(b)
(c)
Nu/Nuo
x/Dh
90°rib
Nu/Nus
Box

List of Figures Captions.

Figure 1: Illustration of forces and main flows features found in a rotating duct

Figure 2: Experimental facility, nomenclature and positions of the PIV measurement planes (highlighted in red)

Figure 3: Measurement set-up used for 2D-PIV on plane xy’ (a) and Stereo-PIV on plane yz

Figure 4: Optical setup sketch and parallax error description

Figure 5: Parallax error compensation for 2D xy’ measurements: examples of calibration by means of dedicated target displacement (a, b) and resulting optical axis position (red dashed lines) and displacement correction fields (c, d)

Figure 6: Comparison of 2D and Stereo-PIV data extracted on the intersection line of xy’ and yz planes of U and V’ profiles from 2D-PIV on xy’ and S-PIV on yz

Figure 7: Stream tracers and contour plot of the in-plane turbulence intensity in plane xy’ for Ro=0.

Figure 8: Stream tracers in plane xy’ for all the rotating cases.

Figure 9: Contour plots of the turbulence intensity in plane xy’ for all the rotating cases.

Figure 10: <uv’>Reynolds stresses component extracted at y’/h=0.5 from plane xy’, (a) static vs Ro = 0.2 and (b) static vs Ro = 0.6 test cases.

Figure 11: Stream tracers (a, b) and contour plots of non-dimensional streamwise velocity component U/U_b (c, d) in plane yz for the smooth channel configuration (Pascotto et al., 2014).

Figure 12: Stream tracers in plane yz for all the rotating cases.

Figure 13: Contour plots of the non-dimensional streamwise velocity component U/U_b in plane yz for all rotating cases.

Figure 14: Tu levels in plane yz for Ro=0.6

Figure 15: Nusselt number ratio distribution in the rotating channel (a – Re = 10000, 400 rpm, b - Re = 30000, 400 rpm) and effect of buoyancy parameter on Nusselt number ratios at x/Dh =4.11 (c) [12]